JACS
JOURNAL OF THE AMERICAN CHEMICAL SOCIETY

ARTICLE

pubs.acs.org/JACS

Vibrational Origin of the Thermal Stability in the High-Performance Piezoelectric Material $GaAsO_4$

O. Cambon,*[†] G. M. Bhalerao,[†] D. Bourgogne,[†] J. Haines,[†] P. Hermet,[‡] D. A. Keen,[§] and M. G. Tucker[§]

[†]Institut Charles Gerhardt Montpellier, UMR-CNRS-UM2-ENSCM-UM1 5253, Université Montpellier 2, Place E. Bataillon, 34095 Montpellier, Cedex 5, France

[‡]Institut Charles Coulomb, UMR-CNRS 5221, Université Montpellier 2, cc026, Place E. Bataillon, 34095 Montpellier Cedex 5, France

[§]ISIS Facility, Rutherford Appleton Laboratory, Harwell Science and Innovation Campus, Didcot, Oxfordshire OX11 0QX, United Kingdom

ABSTRACT: Theoretical calculations and experiments show the absence of libration modes of the tetrahedra in $GaAsO_4$, the most α-quartz-type distorted material. In consequence, the degree of dynamic disorder at high temperature is very low, making $GaAsO_4$ of high interest for high-temperature applications. This paper shows the importance of the theoretical calculations of vibration in oxide materials. In this way, it could be possible to extend this result to other materials and predict the thermal stability of the materials and their potential applications at high temperature.

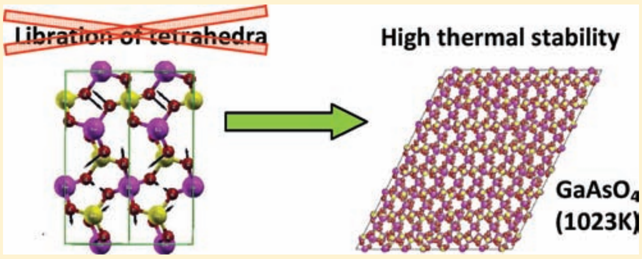

I. INTRODUCTION

The quartz homeotypes $M^{III}X^{V}O_4$ (M^{III} = B, Al, Ga, Fe and X^{V} = P, As) belong to space group $P3_121$ or $P3_221$, and the structure can be described as a helical chain of alternating MO_4 and XO_4 tetrahedra along the z axis. It is possible to quantify the resulting distortion with respect to the β-quartz structure of each material by structural parameters such as the intertetrahedral M−O−X bridging angle θ and tetrahedral tilt angle δ[1,2] of MO_4 (XO_4) tetrahedra about the x axis. The tilt angle is an order parameter for the α-quartz to β-quartz phase transition.[1] An incommensurate phase is present over a 1.4 K temperature range just prior to the appearance of β-quartz.[3] For α-quartz at room temperature $\theta = 143.6°$ and $\delta = 16.4°$, and for β-quartz at 848 K $\theta = 153.3°$ and $\delta = 0°$.[2] On this basis, structure−property relationships have been established between the thermal stability, the physical and piezoelectric properties, and the structural distortion in these materials.[4−14] α-Quartz-type materials having greater structural distortion exhibit better thermal stability and a higher electromechanical coupling coefficient.[6,15] Similarly, the piezoelectric properties of langasite-type materials, some of which are stable up to 1400 °C, increase with the degree of structural distortion[16]

$GaAsO_4$ has been found to have the most distorted structure ($\theta = 129.6°$ and $\delta = 26.9°$) and the highest electromechanical coupling coefficient ($k = 21\%$) among α-quartz-type materials.[6,15] It does not transform to a β-quartz-type phase on heating but decomposes at 1303 K.[15] High-temperature X-ray diffraction studies have shown a high thermal stability of $GaAsO_4$ up to almost the thermal decomposition temperature.[15] A high thermal stability of elastic properties as compared to other α-quartz homeotypes has been found by Brillouin scattering and theoretical studies, which may indicate a similar thermal stability of the piezoelectric properties.[17] Diffraction (X-ray and neutron) studies, Brillouin spectroscopy studies, and density functional theoretical (DFT) investigations provide evidence for a good combination of high thermal stability and high functionality of $GaAsO_4$[6,15,17] up to a temperature of about 1173 K. It can also be noted from these studies that the nonlinear change of structural and other physical properties with temperature for $GaAsO_4$ is significantly smaller than those of $GaPO_4$.[17] These studies provide evidence that $GaAsO_4$ could be the α-quartz-type piezoelectric material with the best piezoelectric performance. However, these studies represent the thermal behavior of the average structure in $GaAsO_4$ and do not give any idea about the dynamic disorder. The thermal response of such a piezoelectric material arises to an important extent from dynamic motion of the constituent tetrahedra. In other materials, the instantaneous local disorder particularly in the oxygen sublattice was shown to be at the origin of the loss of piezoelectric properties well before structural transitions.[14,18,19] Previous studies indicate the possible role of dynamic disorder in the mechanism of the phase transition for SiO_2[20] and $AlPO_4$.[21] In α-quartz, this disorder appears well below the α−β phase transition and is directly related to the loss of piezoelectric properties.[18] The mechanical quality factor Q related to the spectral purity of the resonance of piezoelectric resonators is known to be affected by dynamic disorder. On the other hand, the electromechanical coupling coefficient k is related to the average structure.

Received: March 17, 2011
Published: May 02, 2011

The instantaneous structure of α-quartz-type materials[18,19,22] has been studied previously by total neutron scattering coupled with RMC refinements. The total neutron scattering technique is indeed useful to give the distribution of dynamic atomic configurations at a local level. Model structures refined using the RMC method take into account the experimentally observed total scattering and Bragg scattering and allow the disorder in the instantaneous structure to be visualized both directly and through the distributions of the structurally important bond angles and tetrahedral rotations. The dynamic disorder at high temperature has the effect of rapidly dissipating the induced dipoles, which results in the observed decrease in Q. This happens due to excitation of large amplitude low-frequency rotational modes of rigid tetrahedra. The eigenvector of the libration mode is related to the structural changes at the $\alpha-\beta$ quartz transition. This low-frequency zone-center mode of A_1 symmetry is found at around 205, 295, and 265 cm^{-1} in α-quartz-structured SiO_2,[23,24] $GaPO_4$,[25] and $GaAsO_4$[26], respectively, and has been used to study dynamic disorder. Another higher frequency mode of A_1 symmetry located at around 430 cm^{-1} in $GaAsO_4$[26] is also interesting. This mode can be viewed as bending vibrations of the O−M−O (O−X−O) angle within the MO_4 (XO_4) tetrahedra and is found in the range of 400−500 cm^{-1} for other quartz-type materials for which the $\alpha-\beta$ transition can be detected based on the position and width of this mode.[24]

This paper presents a study of the instantaneous structure and dynamic disorder by total neutron scattering coupled with reverse Monte Carlo modeling. In parallel, Raman spectroscopy as a function of temperature as been performed coupled with theoretical DFT calculations in order to predict the thermal behavior of $GaAsO_4$-based piezoelectric devices.

II. EXPERIMENTAL SECTION

$GaAsO_4$ powder and the single crystal used in the present work were prepared by a hydrothermal method in a poly tetrafluorethylene (PTFE) lined steel autoclave.[10] $Ga(OH)_3$ and H_3AsO_4 were heated in the autoclave at 230 °C. Large single crystals of $GaAsO_4$ were obtained with a slow increase of the temperature for about 3 months. The autoclave was then quenched to obtain the crystals.

II.1. High-Temperature Total Neutron Scattering. *a. Data Acquisition.* Experiments were performed on the time-of-flight (TOF) neutron diffractometer GEM[27] at the ISIS spallation source of the Rutherford Appleton Laboratory (RAL). The powdered sample (2.8 cm^3) was placed in a vanadium can in a furnace and heated from room temperature up to 1023 K. Scattering from the sample was collected using several banks of ZnS scintillator detectors, covering scattering angles 2θ from 6° to 149° and using a TOF range from 0.8 to 20 ms. The scattering vector Q varies from ∼0.1 to 50 $Å^{-1}$. Calibration of the instrument was done using measurements on a vanadium rod, the empty instrument, the empty furnace, and an empty can in the furnace to take all the scattering contributions of the sample environment into account and to normalize the data on an absolute scale. The data were normalized and corrected for absorption to produce powder patterns for Rietveld structure refinements.

b. Rietveld Refinements. The average structure of the samples at each temperature were refined using the program GSAS[28] using the data from four detector banks: bank 3 (centered on $2\theta = 35°$, $1 < d < 5$ Å); bank 4 (centered on $2\theta = 63.6°$, $0.7 < d < 3.714$ Å); bank 5 (centered on $2\theta = 91.3°$, $0.5 < d < 2.385$ Å); bank 6 (centered on $2\theta = 154.4°$, $0.5 < d < 1.765$ Å). The unit cell constants, atomic positions, anisotropic atomic displacement parameters, scale factor, and two line shape parameters were varied in the refinements. Up to 25 background parameters were used to account for background contributions due to diffuse scattering. No restraint was used.

c. Pair Distribution Functions (PDF). The normalized data were combined to obtain the total scattering factor $F(Q)$ at each temperature step. The normalization procedure was carried out using the GUDRUN program, which is based on the ATLAS analysis package.[29] This was followed by Fourier transforming the $F(Q)$ in order to obtain the pair distribution function (PDF) $G(r)$ in terms of the atomic distance r. The PDF is the neutron weighted sum of all the atomic partial pair distances and contains information about the number of atoms of type i around an atom of type j, averaged over all the j atoms.[30]

d. Reverse Monte Carlo Refinements. The RMC modeling,[31] as incorporated within the program RMCProfile,[32] was used to obtain bond angle distributions and the overall disorder within the overall topology of the average structure. The first step for this was to create an (8 × 8 × 4) supercell of the average unit cell. The atoms were then moved randomly and $F(Q)$, $G(r)$, and Bragg diffraction patterns calculated. The difference between the computed and the experimental data was used to determine the acceptability of the random moves until the supercell model yields $F(Q)$, $G(r)$, and Bragg diffraction patterns in good agreement with the experimental data. This instantaneous representation of the structure was then used to calculate correlation functions which provide important additional information with respect to the average structure determined from Rietveld refinement.

II.2. Raman Spectroscopy. *a. Experimental Acquisitions.* Raman spectra were obtained in backscattering geometry using a Horiba Jobin-Yvon LabRam Aramis Raman spectrometer equipped with a diode laser ($\lambda = 473$ nm), an Olympus microscope, and a charge-coupled device camera cooled by a thermoelectric Peltier device. The spectrometer was calibrated using a Si sample. The laser power focused by the objective (×50) of the microscope was about 20 mW on the sample surface. Room-temperature experiments were performed on a [100] $GaAsO_4$ polished plate. For high-temperature measurements, a 2 × 2 × 2 mm^3 single crystal with naturally occurring faces was used. A Linkam TS 1500 heating stage was added to perform high-temperature Raman experiments. The sample was placed on a thin platinum block in the oven of the heating stage to improve the heat flow. At each step, the sample temperature was stabilized for 10 min before measurement. The temperature of the heating stage was calibrated by measuring the temperature of the well-known α-quartz to β-quartz phase transition for SiO_2 ($T_C = 846$ K). The spectra were fitted using a Lorentzian peak profile and a second-order polynomial for the background.

b. Raman Spectra Computational Method. A first-principles study of $GaAsO_4$ was performed within the framework of density functional theory (DFT), as implemented in ABINIT package.[33] Relaxation of internal atomic positions and lattice parameters was performed by using the Broyden−Fletcher−Goldfarb−Shanno algorithm until the maximum residual forces and internal pressure were less than 5×10^{-6} Ha/Bohr and 2×10^{-4} GPa, respectively. The exchange-correlation energy functional was evaluated within the local density approximation using the Perdew−Wang parametrization[34] of Ceperley−Alder homogeneous electron gas data.[35] The all-electron potentials were replaced by norm-conserving pseudopotentials generated according to the Troullier−Martins scheme[36] using a package developed at the Fritz-Haber Institute (Berlin).[37] Ga ($3d^{10}$, $4s^2$, $4p^1$), As ($4s^2$, $4p^3$) and O ($2s^2$, $2p^4$) electrons were considered as valence states in construction of the pseudopotentials. The electronic wave functions were expanded in plane waves up to a kinetic energy cutoff of 65 Ha. Integrals over the Brillouin zone were approximated by sums over a 8 × 8 × 4 mesh of special k points according to the Monkhorst−Pack scheme.[38]

The dynamical matrix yielding the phonon frequencies and eigenvectors was obtained within a variational approach to density functional perturbation theory.[39]

The nonresonant Raman scattering efficiency in a given direction, with a frequency between ω_d and $\omega_d + d\omega_d$ and within a solid angle $d\Omega$ is given for a Stokes process by refs 40 and 41

$$\frac{d^2S}{d\Omega d\varpi_d} = \frac{\omega_d^4}{16\pi^2c^4}[B(\varpi)+1]\hbar \sum_{i,j,k,l} v_i v_k I_{ijkl}(\varpi)\varpi_j\varpi_l \qquad (1)$$

where $\varpi = \omega_0 - \omega_d$ and

$$I_{ijkl}(\varpi) = \sum_m a_{ij}^*(m)a_{kl}(m)\frac{1}{2\varpi_m}[\delta(\varpi-\varpi_m) - \delta(\varpi+\varpi_m)] \qquad (2)$$

In these equations (i, j, k, l) indices denote the Cartesian components, the asterisk symbolizes the complex conjugate, c is the speed of light in the medium, $\hbar$ is the reduced Planck constant, ω_0 (respectively, ω_d) is the frequency of incident (respectively, scattered) light, v (respectively, ω) is the polarization unit vector of the incident (respectively, scattered) light, $B(\omega)$ is the Bose factor, and ω_m is the frequency of the mth zone-center phonon mode. The Raman susceptibility tensor is defined as

$$a_{ij}(m) = \sqrt{\Omega_0}\sum_{\kappa,\gamma}\pi^{\kappa}_{ij,\gamma}u_m(\kappa\gamma) \qquad (3)$$

where the sum runs over all atoms κ and space directions γ, $u_m(\kappa\gamma)$ is the $(\kappa\gamma)$ component of the mth phonon eigen displacement vector, and $\tilde{\pi}$ is a third-rank tensor describing the changes of the linear dielectric susceptibility induced by an individual atomic displacement defined as

$$\pi^{\kappa}_{ij,\gamma} = \left.\frac{\partial\chi^{(1)}_{ij}}{\partial\tau_{\kappa\gamma}}\right|_0 \qquad (4)$$

where $\tau_{\kappa\gamma}$ corresponds to the displacement of the κth atom in the direction γ.

Within the DFT framework, $\pi^{\kappa}_{ij,\gamma}$ tensors are related to a mixed third-order derivative with respect to two electric fields and one atomic displacement of the field-dependent energy functional, $F = E - \Omega_0\varepsilon.P$, as defined in ref 42, where E is the total energy in zero field and ε (respectively, P) is the macroscopic electric field (respectively, polarization)

$$\pi^{\kappa}_{ij,\gamma} = -\frac{1}{\Omega_0}\frac{\partial^3F}{\partial\varepsilon_i\partial\varepsilon_j\partial\tau_{\kappa\gamma}} \qquad (5)$$

These derivates are evaluated at the equilibrium atomic positions and under the condition of zero electric field (respectively, displacement field) for transverse (respectively, longitudinal) optic phonon modes. They were obtained within a nonlinear response formalism taking advantage of the $(2n + 1)$ theorem as described in ref 43.

Table 1. Unit Cell Parameters, Volume and Agreement Factors for $GaAsO_4$ as a Function of Temperature[a]

T (K)	a (Å)	c (Å)	V (Å^3)	R_{wp}	R_p	χ^2
303	4.99705(2)	11.38722(7)	246.250(2)	0.0383	0.0451	5.12
723	5.03044(2)	11.40295(8)	249.896(3)	0.0331	0.0401	3.68
1023	5.05834(3)	11.41673(9)	252.981(3)	0.0295	0.0348	1.73

[a] Agreement factors are defined as follows, $R_{wp} = ((w(Y_{obs} - Y_{calcd})^2)/\Sigma(wY^2_{obs}))^{1/2}$, $R_p = (\Sigma|Y_{obs} - Y_{calcd}|)/(\Sigma Y_{obs})$, and $\chi^2((w(Y_{obs} - Y_{calcd})^2)/(N_{obs} - N_{var}))$, where N_{obs} is the number of observed points and N_{var} the number of variables.

III. RESULTS AND DISCUSSION

III.1. Average Structures—Rietveld Refinements. Rietveld refinements (Tables 1, 2, and 3 and Figure 1) confirmed the extreme thermal stability of $GaAsO_4$.[15,17] The results are in very good agreement with previous X-ray diffraction studies.[6,15] Due to the same electronic configuration of the heavy Ga^{3+} and As^{5+} ions (with similar X-ray scattering factors), it is difficult to distinguish Ga and As using X-ray diffraction. Moreover, the X-ray scattering factor of O atoms is relatively very weak, which leads to higher uncertainties in the O-atom positions and atomic displacement parameters. The neutron scattering lengths for Ga, As, and O atoms are 7.288×10^{-13}, 6.58×10^{-13}, and 5.803×10^{-13} cm, respectively, and hence, the relative contribution of the O sublattice is much greater than in X-ray scattering. When compared to $GaPO_4$ the equivalent atomic displacements parameters at 1023 K are similar (about 2×10^{-2} Å^2 for the cations and about 4×10^{-2} Å^2 for O atoms). Ga−O and As−O bond lengths and O−Ga−O and O−As−O angles are also obtained from the Rietveld refinements; based on these the thermal behavior of the average structure of $GaAsO_4$ behaves in a similar way to $GaPO_4$. Upon increasing the temperature from RT to 1023 K, the mean values of the internal angles of GaO_4 and AsO_4 tetrahedra do not vary and are equal to 109.5°. Only the width of the distributions decreases from 8.2° to 7.2° for GaO_4 and from 5.6° to 2.7° for AsO_4. These decreases in the widths of distributions with temperature are of the same order as the increase in the intertetrahedral θ angle (θ_{RT} = 129.8° and θ_{1023K} = 132.7°). Upon increasing the temperature, the tetrahedra become more symmetric and the distortion decreases slightly, indicating that instead of tilting of rigid tetrahedral, thermal behavior is linked to changes in both the inter- and the intratetrahedral bond angles.

III.2. Total Neutron Scattering: Instantaneous Structure. Pair distribution functions $G(r)$ were obtained from the total neutron scattering functions $F(Q)$ at each temperature and are plotted in Figure 2 as $rG(r)$. The first two peaks represent As−O and Ga−O distances, respectively. These distances were determined by Gaussian peak profile fitting. The room-temperature values (1.678 Å for As−O and 1.833 Å for Ga−O) are comparable to those obtained on Rietveld refinement of the present neutron scattering data (1.670 and 1.827 Å) and those previously obtained from X-ray diffraction (1.6675 and 1.8305 Å).[6] These distances are plotted as a function of temperature in Figure 3. The distances between two oxygen atoms belonging to same AsO_4- or GaO_4-type tetrahedron are about 2.7 and 3.0 Å, respectively. This group of distances between 2.6 and 3.8 Å includes the intertetrahedral distances between atoms (Ga−As, Ga−O, As−O, and O−O pairs). The inset in Figure 2 indicates

Table 2. Fractional Atomic Coordinates and Equivalent Atomic Displacement Parameters U_{eq} (Å^2) for $GaAsO_4$ as a Function of Temperature[a]

T (K)	x_{Ga}	$100 \times U_{eq}$	x_{As}	$100 \times U_{eq}$	x_{O1}	y_{O1}	z_{O1}	$100 \times U_{eq}$	x_{O2}	y_{O2}	z_{O2}	$100 \times U_{eq}$
303	0.4515(2)	0.38(5)	0.4473(3)	0.51(5)	0.3999(3)	0.3171(2)	0.38380(6)	0.88(5)	0.3985(3)	0.2934(2)	0.87198(7)	0.96(5)
723	0.4544(3)	1.33(1)	0.4493(4)	1.43(1)	0.4027(5)	0.3126(3)	0.38483(8)	2.64(1)	0.4002(5)	0.2891(3)	0.8733(1)	2.51(1)
1023	0.4597(4)	2.05(1)	0.4477(5)	2.3(3)	0.4122(5)	0.3097(4)	0.3853(1)	4.47(1)	0.3948(4)	0.2846(4)	0.8749(1)	3.73(1)

[a] In the $P3_121$ space group Ga is placed in $3a$ $(x,0,1/3)$ sites, As is in $3b$ $(x,0,5/6)$ sites, and O1 and O2 are each in $6c$ (x,y,z) sites. U_{eq} is defined as 1/3 the trace of the diagonalized matrix of the u_i components of an equivalent ellipsoid defined with orthogonal axes.

Table 3. Atomic Displacement Parameters ($Å^2$) for $GaAsO_4$ from Anisotropic Rietveld Refinements

	Ga						As					
T (K)	$100 \times U_{11}$	$100 \times U_{22}$	$100 \times U_{33}$	$100 \times U_{12}$	$100 \times U_{13}$	$100 \times U_{23}$	$100 \times U_{11}$	$100 \times U_{22}$	$100 \times U_{33}$	$100 \times U_{12}$	$100 \times U_{13}$	$100 \times U_{23}$
303	0.47(4)	0.43(6)	0.24(4)	0.21(3)	0.04(2)	0.08(4)	0.77(5)	0.73(7)	0.03(5)	0.36(3)	0.03(2)	0.06(5)
723	1.43(8)	1.1(1)	1.34(8)	0.55(5)	0.02(4)	0.03(8)	1.76(8)	1.9(1)	0.67(8)	0.97(6)	0.04(4)	0.08(9)
1023	2.4(1)	1.0(1)	2.3(1)	0.50(5)	−0.01(4)	−0.02(8)	2.6(1)	3.3(1)	1.3(1)	1.65(7)	0.07(6)	0.1(1)

	O1						O2					
T (K)	$100 \times U_{11}$	$100 \times U_{22}$	$100 \times U_{33}$	$100 \times U_{12}$	$100 \times U_{13}$	$100 \times U_{23}$	$100 \times U_{11}$	$100 \times U_{22}$	$100 \times U_{33}$	$100 \times U_{12}$	$100 \times U_{13}$	$100 \times U_{23}$
303	1.35(6)	1.10(5)	0.60(3)	0.93(5)	−0.36(3)	−0.45(3)	1.78(7)	0.97(5)	0.49(3)	0.96(5)	−0.46(4)	−0.47(3)
723	4.5(1)	2.92(9)	1.64(6)	2.7(1)	−1.16(6)	−1.30(6)	3.9(1)	2.56(9)	2.06(5)	2.3(1)	−1.10(7)	−1.27(7)
1023	9.0(2)	4.0(1)	2.28(8)	4.7(1)	−1.98(9)	−1.76(8)	3.8(1)	4.5(1)	3.51(8)	2.6(1)	−1.30(9)	−2.12(9)

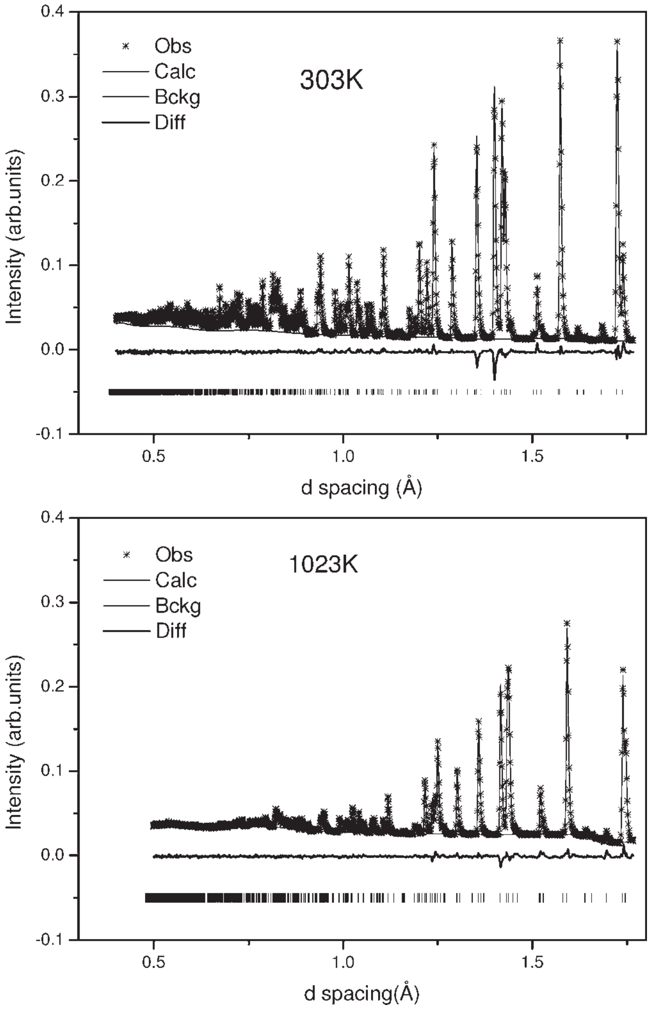

Figure 1. Experimental and calculated profiles from the Rietveld refinements of neutron powder diffraction for $GaAsO_4$ at 303 and 1023 K. Only one (centered on $2\theta = 154.4°$) of the four detector banks of refined data is shown. Vertical tick marks correspond to the positions of the Bragg reflections calculated from the refined structural model.

that the nearest neighbor As—O and Ga—O distances increase only slightly with temperature. The difference in the values obtained from Rietveld refinement and the pair distribution function (Figure 3) arises due to the different procedure of determination of bond lengths in the two techniques. In the Rietveld refinement, these are calculated as the difference between average atom positions in the average structure, whereas the PDF is directly determined from Fourier transforming the total neutron scattering data and corresponds to a direct measurement of the separation of atom pairs. For the bonds with the pentavalent cation X^V (P^V or As^V for $GaPO_4$[19] and $GaAsO_4$), the evolution the X—O bonds versus temperature is in good agreement for Rietveld and PDF refinements. Nevertheless, upon comparing the evolution of the Ga—O bond for both materials, the Rietveld refinements lead to a decrease in the length with temperature which is unphysical behavior for these materials. In the case of $GaPO_4$,[19] the average structure was shown not to be realistic, because it does not take account of the effect of the dynamic disorder. However, the relative error between PDF and Rietveld refined values for the Ga—O bond length due to the dynamic disorder at 1023 K is less marked for $GaAsO_4$ (1.5%) than for $GaPO_4$ (2%). This is a sign that the dynamic disorder is less important in $GaAsO_4$. This result indicates that excitation of low-energy modes is less important in $GaAsO_4$, proving that the dynamic disorder is the lowest in $GaAsO_4$ as compared to other quartz-type materials.[19,20,22,44,45]

III.3. RMC Modeling: Instantaneous Topology. Projection of the RMC-modeled instantaneous snapshot of the crystal structure of $GaAsO_4$ along the crystallographic *c* axis is shown in Figure 4 at room temperature and 1023 K. Little disorder is observed in the O sublattice. The instantaneous structure shows a remarkable absence of dynamic disorder in $GaAsO_4$ as compared to $GaPO_4$[19] and α-quartz.[46] Figure 5 shows the distribution of the intertetrahedral bridging angle θ (Ga—O—As) in $GaAsO_4$ as a function of temperature. These calculated distributions were fitted to a Gaussian profile in order to obtain the mean value and the width of the distribution (Figure 5 and Table 4).

Distributions of tetrahedral tilt angle δ values were also obtained from RMC calculations (Table 4). The relative decrease of the δ angles in the same temperature range is 5.7% and 3.5% for GaO_4 and AsO_4, respectively, in $GaAsO_4$, whereas the decrease is 13% and 5.4% for GaO_4 and PO_4 in $GaPO_4$.[19] Even if the δ angles are similar at room temperature for the pentavalent cation-centered PO_4 and AsO_4 tetrahedra, we observe that the δ value for the trivalent cation-centered GaO_4 tetrahedron changes more with temperature in $GaPO_4$ than in $GaAsO_4$. This effect is most probably related to the polarization properties of the

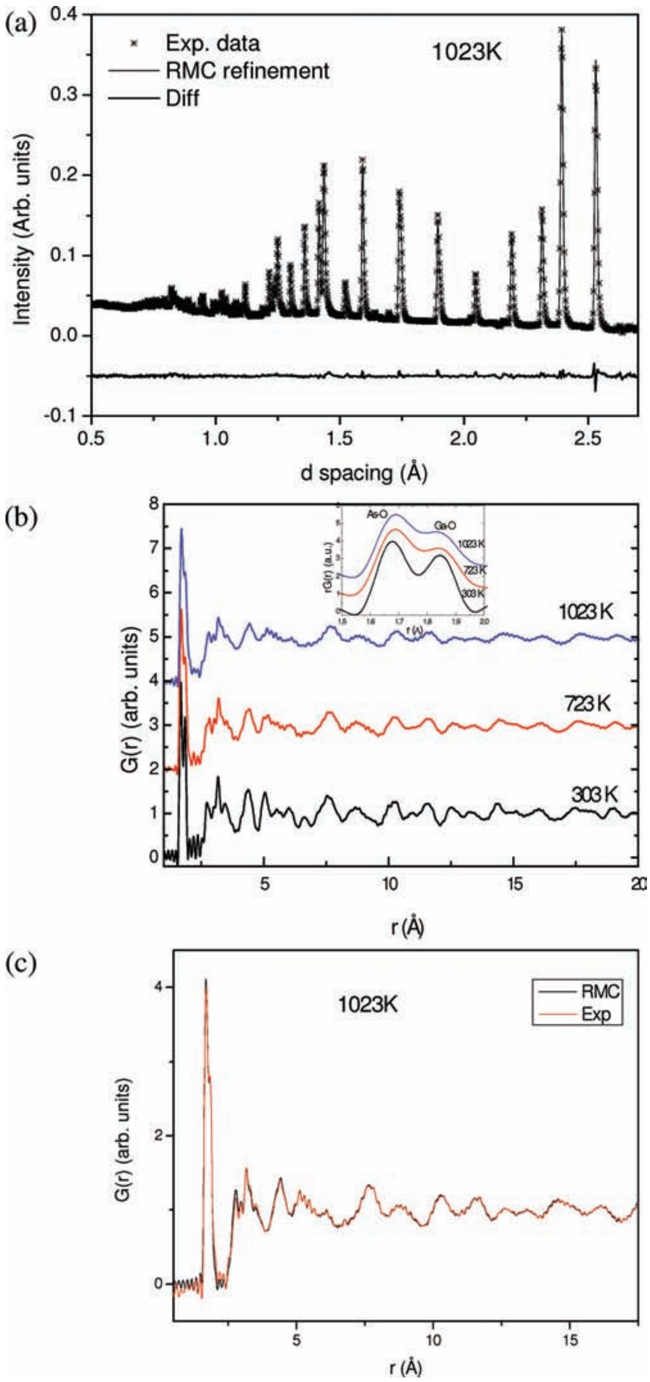

Figure 2. (a) Bragg peaks RMC refinements at 1023 K. (b) Experimental $GaAsO_4$ pair distribution functions from total neutron scattering as a function of temperature. (c) RMC fit of $G(r)$ data at 1023 K.

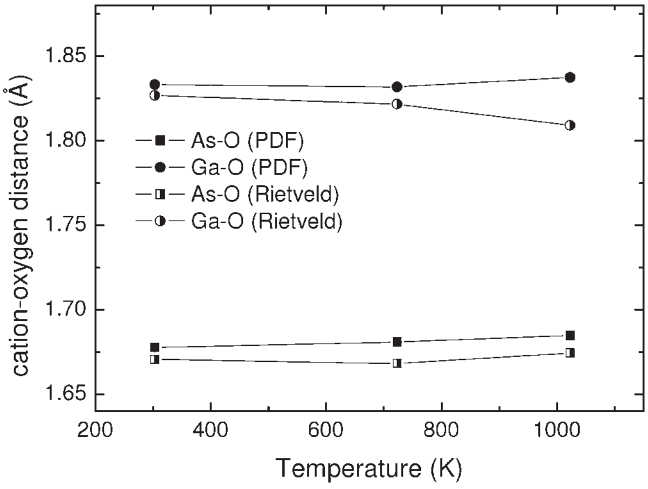

Figure 3. Intratetrahedral cation−oxygen distances determined from pair distribution functions derived from total neutron scattering in comparison with Rietveld refinements from neutron diffraction data for $GaAsO_4$ as a function of temperature.

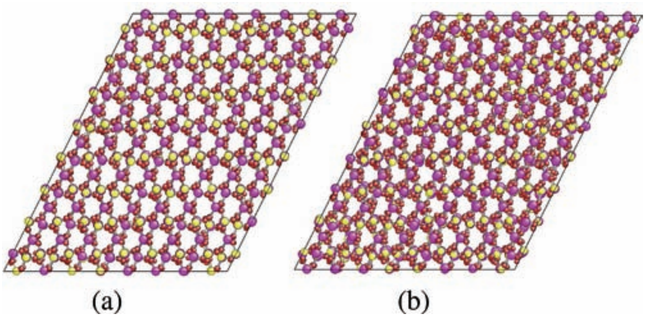

Figure 4. Instantaneous structure of $GaAsO_4$ refined by RMC and viewed along the crystallographic [001] direction at room temperature (a) and at 1023 K (b). O atoms in red, Ga atoms in yellow, and As atoms in violet.

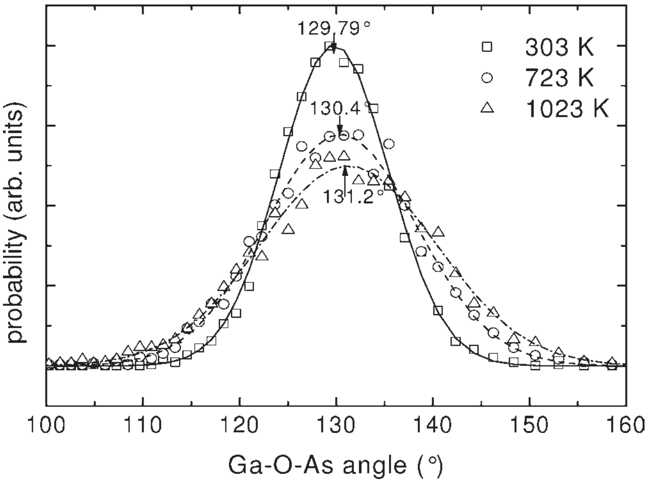

Figure 5. Distribution of θ (Ga−O−As) angles determined by RMC refinements for $GaAsO_4$ as a function of temperature.

cation−oxygen bonds in the individual tetrahedra. The partial charges developed on the cations (at 0 K) have been calculated from density functional theory (DFT) for $GaAsO_4$ and $GaPO_4$.[17] The partial charge developed on the trivalent and pentavalent cation is +1.57 (Ga) and +0.9 (As), respectively. On the other hand, these values are +1.62 (Ga) and +2.12 (P) in the case of $GaPO_4$. The partial charge on the Ga cation is almost identical in $GaPO_4$ and $GaAsO_4$. Moreover, the δ angle value at room temperature is similar for the pentavalent P and As tetrahedra in both materials. The influence of the As atom is observed on the neighboring O atoms, which are less charged in the case of $GaAsO_4$ ($q_{O1/O2} = -0.633/-0.602$)[17] than in $GaPO_4$ ($q_{O1/O2} = -0.927/-0.945$).[17] We observe here clearly the influence

Table 4. Tilt Angles δ and Intertetrahedral Bridging Angles θ of $GaAsO_4$ Obtained by Using Classical Rietveld Refinement (averaged structure) Compared to Angle Distributions Obtained by Using RMC Refinements (instantaneous topology) as a Function of Temperature

	δ_{GaO4} (deg)		δ_{AsO4} (deg)		$\theta_{Ga-O-As}$ (deg)	
T (K)	Rietveld	RMC distribution average/width	Rietveld	RMC distribution average/width	Rietveld	RMC distribution average/width
303	24.98	24.58/4.56	27.87	25.60/5.6	129.8(1)	129.79/11.4
723	24.08	24.02/7.65	26.73	25.11/7.43	131.3(1)	130.4/15.7
1023	23.85	23.17/8.85	25.12	24.74/8.54	132.7(1)	131.2/18.2

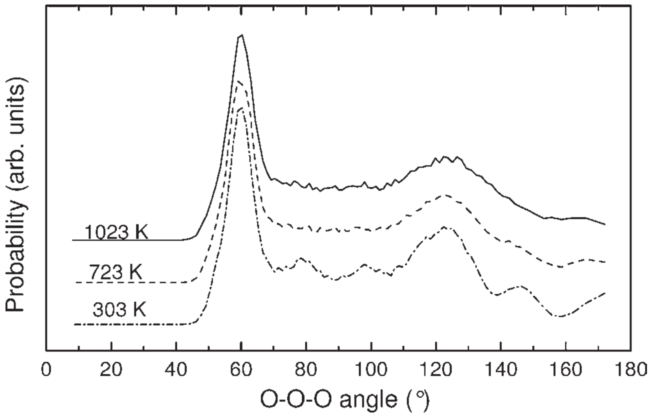

Figure 6. Distribution of O−O−O angles obtained from RMC refinements for $GaAsO_4$ as a function of temperature.

of the chemical bond on the thermal stability of the material. A smaller partial charge on the shared atoms of the cation−oxygen bond is an indication of the higher covalent character of the bond. The increase in the average distortion is lower at high temperature for more covalent materials. This observation is in agreement with a previous study on the α-quartz-type solid solution $Al_{(1-x)}Ga_xPO_4$, which showed that a higher degree of covalent bonding with oxygen reduces dynamic disorder at higher temperature.[22] The predominantly covalent nature of bonding in $GaAsO_4$ is expected to give more directionality and rigidity to the structure, thereby decreasing dynamic disorder and increasing its thermal stability. The dynamic disorder is related to the excitation of large amplitude rigid-unit modes in the tetrahedra-based framework structure. These modes give rise to the width of instantaneous distributions of tetrahedral tilt angles obtained from RMC (Table 4).

Figure 6 shows the O−O−O bond angle distribution obtained from RMC calculations. The sharp peak centered around 60° corresponds to the intratetrahedral angle, which hardly shows any change with temperature. The higher angle distributions represent several intertetrahedral configurations, and the width of these distributions increases with temperature due to the increasing dynamic disorder present in the lattice. The intense peak located at about 122° corresponds to the angle between the nearest edges of two corner-sharing tetrahedra. The broadening in this intertetrahedral O−O−O feature is a sign of increased dynamic disorder on increasing temperature. However, the dynamic disorder is lower as compared to that in $GaPO_4$.[19] We also observe (Figure 6) that the two other peaks located at about 77° and 98° broaden quickly with temperature, as compared to the peaks located at 60° and 122°. These intermediate O−O−O angles arise from tetrahedra, which are not nearest neighbors. Although it is not very straightforward to interpret these distributions in terms of tetrahedral rigid unit modes, it can be seen that these peaks lose intensity relatively slowly in the case of $GaAsO_4$ as compared to $GaPO_4$.[19]

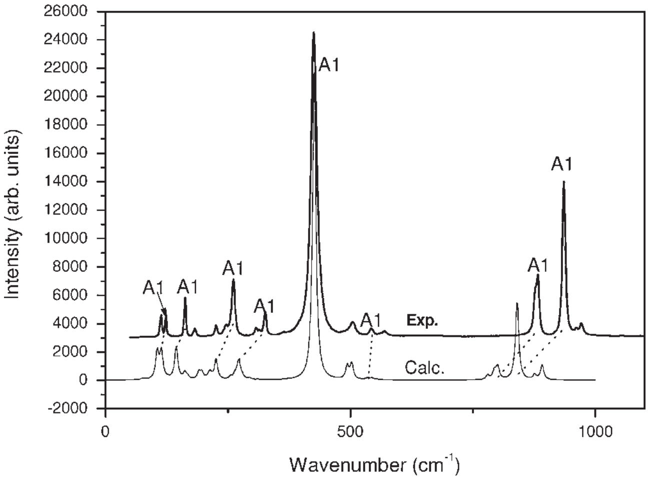

Figure 7. Experimental and average calculated Raman spectrum of $GaAsO_4$.

III.4. Raman Spectroscopy. $GaAsO_4$ belongs to space group $P3_121$ or $P3_221$ with $Z = 3$. In this case, group theory predicts 54 modes of vibration: $\Gamma = 8A_1 + 10A_2 + 18E$ of which $1A_2 + 1E$ are acoustic modes; E modes are double-degenerate modes. The remaining modes are optical: $\Gamma_{optic} = 8A_1 + 9A_2 + 17E$, and the following modes are active in Raman

$$\Gamma(\text{Raman}) = 8A_1 + 17E$$

III.4.1. Raman Spectroscopy at Room Temperature. The experimental Raman spectrum from a [100] $GaAsO_4$ plate without any polarized light is compared to the averaged calculated spectrum obtained from partial spectra computed along all directions (Figure 7). All calculated modes are reported in Table 5, which allows the modes of the experimental spectrum to be assigned. The modes were assigned based on their wavenumber and intensity. Eight A_1 and 14E modes have been identified in the experimental spectrum. The calculated low-frequency mode at 226 cm^{-1} involving only oxygen displacements is illustrated (Figure 8). The corresponding oxygen displacements mode in quartz SiO_2 involves the libration of the SiO_4 tetrahedra, which is responsible of the α−β transition. This movement is a tilting of the tetrahedra round the x axis, and the O atoms rotate in the (y, z) plane with identical components.[23] For $GaAsO_4$, the A_1 mode is not a libration but a more complex mode where the O atoms have two different

Table 5. Wavenumber (cm^{-1}) of the Observed Modes (±1 cm^{-1}) in the Raman Spectrum of $GaAsO_4$ at 293 K Compared to the Average Calculated Modes

modes symmetry	average calculated spectrum (0 K) wavenumber (cm^{-1})	experimental spectrum (293 K) wavenumber (cm^{-1})
E TO1 (LO1)	75 (77)	
E TO2 (LO2)	105 (106)	113
*A*1	114	123
E TO3 (LO3)	128 (128)	130
*A*1	144	162
E TO4 (LO4)	162 (167)	183
E TO5 (LO5)	191 (197)	225
E TO6 (LO6)	211 (214)	245
*A*1	226	260
E TO7 (LO7)	255 (264)	307
E TO8 (LO8)	270 (279)	314
A_1	272	325
E TO9 (LO9)	294 (312)	364
*A*1 (intratetrahedral bending)	426	425
E TO10 (LO10)	439 (440)	
E TO11 (LO11)	493 (502)	505
*A*1	534	542
E TO12 (LO12)	543 (552)	569
E TO13 (LO13)	552 (556)	634
E TO14 (LO14)	780 (793)	
E TO15 (LO15)	795 (835)	877
*A*1	800	882
E TO16	837	
*A*1	840	935
E LO16	876	961
E TO17 (LO17)	891 (892)	971

components in different planes, implying bending of the intratetrahedral angles. The absence of a libration mode and consequent instability is an important result, which explains why this material is extremely stable with no α−β transition and a very low dynamic disorder as shown by total neutron scattering study.

III.4.2. High-Temperature Raman Spectroscopy: Dynamic Disorder. Raman spectra from single-crystal $GaAsO_4$ on heating to 1186 K and subsequent cooling are shown (Figure 9). Increasing temperature results in a progressive change in wavenumber and line width (full width at half maxima, fwhm) of Raman modes. Figure 10 shows the thermal evolution of the position of the Raman peaks. The frequencies of all modes decrease with increasing temperature. The most important low-wavenumber feature for the thermal stability located at ~261 cm^{-1} is circled in Figure 10. This A_1 symmetry mode, which is not a libration in $GaAsO_4$, does not show mode softening found in other α-quartz homeotypes like SiO_2 or $AlPO_4$, which undergo an α-quartz to a β-quartz phase transition. As noted previously, $GaAsO_4$ does not undergo a phase transition but decomposes on heating.[15] The midfrequency mode situated at ~425 cm^{-1} is an intratetrahedral oxygen−cation−oxygen bending mode (also circled in Figure 10). The wavenumber shift and line width of this mode have been used in order to follow the α−β phase transformation in quartz-type materials.[24,47−52] In $GaAsO_4$, this mode is particularly stable as a function of temperature.

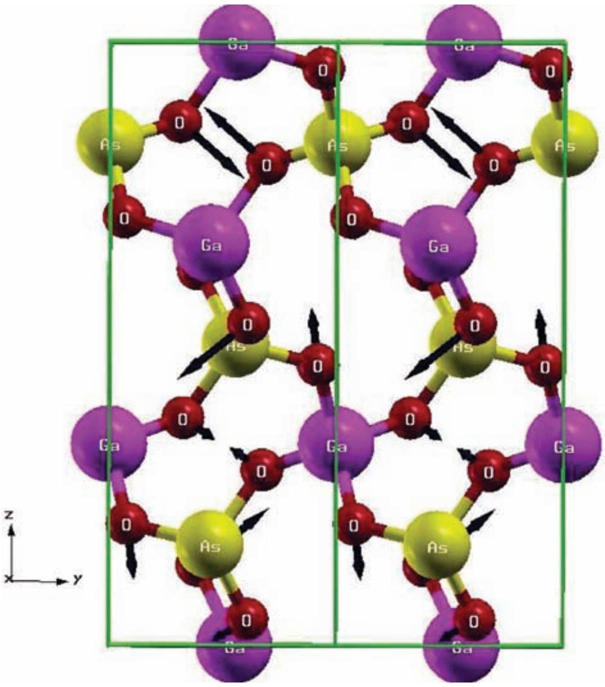

Figure 8. Calculated A_1 mode at 226 cm^{-1}.

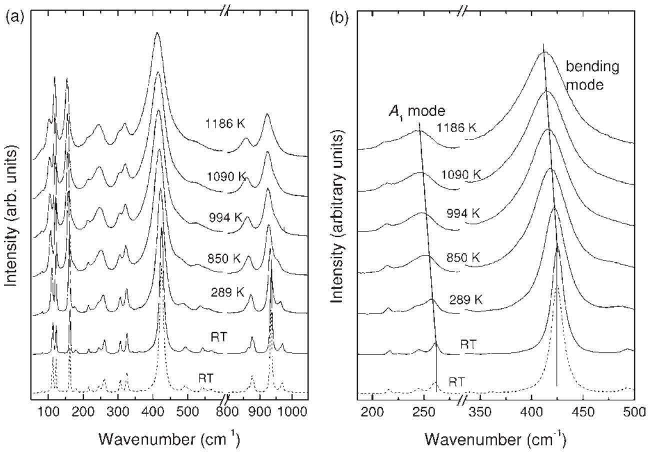

Figure 9. (a) Experimental Raman spectra of α-quartz-type $GaAsO_4$ as a function of temperature. Spectrum on cooling back to room temperature is shown as the dashed curve. (b) A_1 mode at 260 cm^{-1} and bending modes at 425 cm^{-1} are shown in detail.

The wavenumber of the A_1 mode near 260 cm^{-1} decreases up to the maximum temperature obtained of 1186 K (Figure 10) with the first two thermal coefficients being -1.6×10^{-2} and 3.6×10^{-6} cm^{-1} K^{-2} for a wavenumber shift of 9 cm^{-1}. These coefficients are comparable to those of the bending mode (-0.8×10^{-2} and -4.2×10^{-6} cm^{-1} K^{-2}) for a wavenumber shift of 13 cm^{-1}. This observation is a direct indication of the excellent thermal stability of the structural distortion in $GaAsO_4$, which is responsible for the thermal stability of the physical properties observed experimentally[17] and as predicted on the basis of structure-physical properties relationships.[5] Damping Γ_T

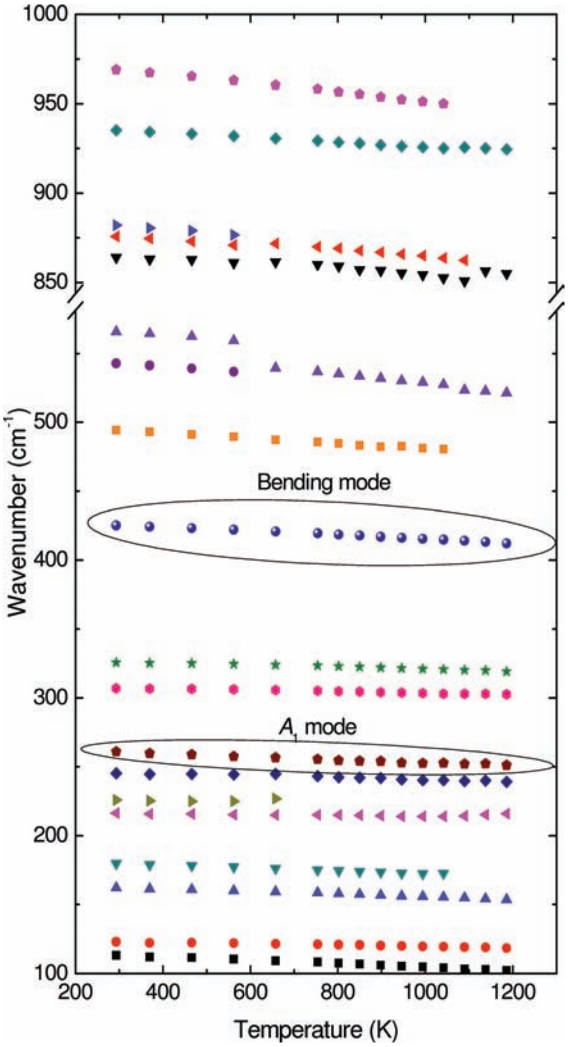

Figure 10. Position of Raman modes of $GaAsO_4$ as a function of temperature.

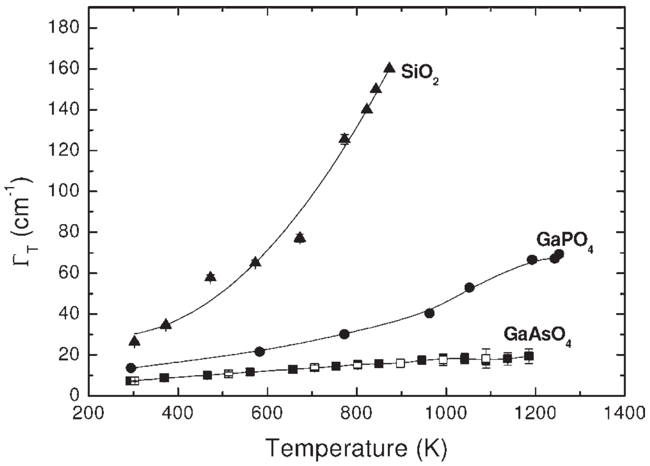

Figure 11. Width of the Raman active A_1 mode located at 261 cm^{-1} of $GaAsO_4$ as a function of temperature. Values for α-$GaPO_4$[23] and α-quartz-structured SiO_2[22] are shown for comparison. Filled and empty symbols for $GaAsO_4$ correspond to the measurements during heating and cooling cycles, respectively.

of this mode, represented by the line width (fwhm), increases as a function of temperature (Figure 11). Damping of the libration modes for α-quartz-structured SiO_2 and $GaPO_4$ are also shown for comparison. We observe that at room temperature the damping is the lowest (7 cm^{-1}) for $GaAsO_4$ as compared to $GaPO_4$ (13.6 cm^{-1}) and α-quartz (26.4 cm^{-1}). In the quartz homeotype materials, the transition to the β-quartz-type phase is linked in particular to tetrahedral tilting. The order parameter for the α-quartz to β-quartz phase transition is the rotation of the SiO_4 tetrahedra about their 2-fold symmetry axis, corresponding to the tetrahedral tilt angle δ. The eigenvector of the libration mode also corresponds to rotation of tetrahedra related to the structural α−β transition for SiO_2. The instability of this mode is clearly observed in the α−β transition of quartz by a sharp increase in the line width and a decrease in wavenumber from well below the transition temperature. Increased damping of this mode is also observed in $GaPO_4$, notably from about 200 K below the maximum temperature of existence of α-quartz phase, although it is less pronounced as for α-quartz-structured SiO_2. $GaPO_4$ does not exhibit a α−β quartz transition, but it transforms to a β-cristobalite structure. In contrast to $GaPO_4$ and SiO_2, the increase of damping on heating is very small for $GaAsO_4$. Increased damping of the libration mode can be related to increased instability in the structure due to dynamic disorder. This implies that the anharmonicity in $GaAsO_4$ does not increase significantly even up to about 100 K below the thermal decomposition temperature and is entirely consistent with the fact that this mode is not a libration in $GaAsO_4$. These results further corroborate the findings from neutron scattering and RMC modeling. All these results show that for $GaAsO_4$ the high degree of distortion implies that the bonds with the oxygen atoms are more covalent. The four sp^3 orbitals around the O atoms thus tend toward tetrahedral geometry. The structure is more rigid and the tetrahedra are more strongly interconnected, thus eliminating librational motion. In consequence, no dynamic disorder and no (α−β) quartz transition are observed.

IV. CONCLUSION

Total neutron scattering studies coupled with RMC refinements and Raman spectroscopic studies have been performed on $GaAsO_4$ as a function of temperature up to 1186 K. It was found that $GaAsO_4$ has the highest thermal stability among materials with the α-quartz-type structure. Dynamic disorder was found to be very low at room temperature and does not increase as much as in other materials at high temperature. Raman spectra calculated by DFT represent very important progress in the better understanding of the thermal stability in the α-quartz materials. In the case of highly distorted materials like $GaAsO_4$, the chemical bonds in the tetrahedra are highly covalent and the low-frequency A_1 mode does not have a libration character. The material thus does not present the instability which gives rise to the α−β transition. This result provides the physical origin of the low degree of dynamic disorder in this material. In going from $GaPO_4$ to $GaAsO_4$, the pentavalent cation P is replaced by As, improving the covalent character of the chemical bonds, thereby reducing the dynamic disorder at elevated temperature. As it has been already shown for other materials, reduced dynamic disorder results in better coherence in the relative orientations of adjacent dipoles induced under the effect of external electric field. $GaAsO_4$ can thus be expected to exhibit very stable piezoelectric properties such as the quality factor Q at high temperature.

Moreover, DFT calculations of vibrational modes could be extended to other classes of materials to predict their high-temperature behavior and thus can be used for conception of higher performance materials for a wide variety of applications.

■ AUTHOR INFORMATION

Corresponding Author
olivier.cambon@univ-montp2.fr

■ ACKNOWLEDGMENT

The authors would like to thank the ANR for financial support (contract no. ANR-07-BLAN0258-PIEZOCRIST).

■ REFERENCES

(1) Grimm, H.; Dorner, B. *J. Phys. Chem. Solids* **1975**, *36*, 413.
(2) Kihara, K. *Eur. J. Mineral* **1990**, *2*, 63.
(3) Dolino, G. *Incommensurate Phases in Dielectrics*; Blinc, R., Levanyuk, A. P., Eds.; North Holland: Amsterdam, 1986; Vol. II, pp 206−232.
(4) Philippot, E.; Goiffon, A.; Ibanez, A.; Pintard, M. *J. Solid State Chem.* **1994**, *110*, 356.
(5) Philippot, E.; Palmier, D.; Pintard, M.; Goiffon, A. *J. Solid State Chem.* **1996**, *123*, 1.
(6) Philippot, E.; Armand, P.; Yot, P.; Cambon, O.; Goiffon, A.; McIntyre, G. J.; Bordet, P. J. *Solid State Chem.* **1999**, *146*, 114.
(7) Haines, J.; Chateau, C.; Léger, J. M.; Marchand, R. *Ann. Chim. Sci. Mater.* **2001**, *26*, 209.
(8) Haines, J.; Cambon, O.; Philippot, E.; Chapon, L.; Hull, S. *J. Solid State Chem.* **2002**, *166*, 434.
(9) Haines, J.; Cambon, O.; Hull, S. *Z. Kristallogr.* **2003**, *218*, 193.
(10) Cambon, O.; Yot, P.; Rul, S.; Haines, J.; Philippot, E. *Solid State Sci.* **2003**, *5*, 469.
(11) Cambon, O.; Haines, J. *Proceedings of the 2003 IEEE International Frequency Control Symposium & 17th European Frequency and Time Forum*; Tampa, FL, May 8, 2003; IEEE: Piscataway, NJ, 2003; p 650.
(12) Haines, J.; Cambon, O.; Astier, R.; Fertey, P.; Chateau, C. *Z. Kristallogr.* **2004**, *219*, 32.
(13) Haines, J.; Cambon, O. *Z. Kristallogr.* **2004**, *219*, 314.
(14) Cambon, O.; Haines, J.; Fraysse, G.; Keen, D. A.; Tucker, M. G. *J. Phys. IV* **2005**, *126*, 27.
(15) Cambon, O.; Haines, J.; Fraysse, G.; Détaint, J.; Capelle, B.; Van der Lee, A. *J. Appl. Phys.* **2005**, *97*, 074110.
(16) Mill, B. V. ; Pisarevsky, Y. V. *Proceedings of the IEEE/EIA International Frequency Control Symposium and Exhibition*; Kansas City, 2000; p 133.
(17) Bhalerao, G. M.; Cambon, O.; Haines, J.; Levelut, C.; Mermet, A.; Sirotkin, S.; Menaert, B.; Debray, J.; Baraille, I.; Darrigan, C.; Rerat, M. *Inorg. Chem.* **2010**, *49*, 9470.
(18) Haines, J.; Cambon, O.; Keen, D. A.; Tucker, M. G.; Dove, M. T. *Appl. Phys. Lett.* **2002**, *81*, 2968.
(19) Haines, J.; Cambon, O.; Prudhomme, N.; Fraysse, G.; Keen, D. A.; Chapon, L. C.; Tucker, M. G. *Phys. Rev. B* **2006**, *73*, 014103.
(20) Tucker, M. G.; Keen, D. A.; Dove, M. T. *Mineral. Mag.* **2001**, *65*, 489.
(21) Gregora, I.; Magneron, N.; Simon, P.; Luspin, Y.; Raimboux, N.; Philippot, E. *J. Phys.: Condens. Matter* **2003**, *15*, 4487.
(22) Cambon, O.; Haines, J.; Cambon, M.; Keen, D. A.; Tucker, M. G.; Chapon, L.; Hansen, N. K.; Souhassou, M.; Porcher, F. *Chem. Mater.* **2009**, *21*, 237.
(23) McMillan, P. F.; Hess, A. C. *Phys. Chem. Miner.* **1990**, *17*, 97.
(24) Ranieri, V.; Bourgogne, D.; Darracq, S.; Cambon, M.; Haines, J.; Cambon, O.; Le Parc, R.; Levelut, C.; Largeteau, A.; Demazeau, G. *Phys. Rev. B* **2009**, *79*, 224304.
(25) Angot, E.; Le Parc, R.; Levelut, C.; Beaurain, M.; Armand, P.; Cambon, O.; Haines, J. *J. Phys.: Condens. Matter* **2006**, *18*, 4315.
(26) Dultz, W.; Quilichini, M.; Scott, J. F.; Lehmann, G. *Phys. Rev. B* **1975**, *11*, 1648.
(27) Hannon, A. C. *Nucl. Instrum. Methods Phys. Res. A* **2005**, *551*, 88.
(28) Larson, A. C.; Von Dreele, R. B. *GSAS: General Structure Analysis System*; Los Alamos National Laboratory: Los Alamos, NM, 1994.
(29) Hannon, A. C.; Howells, W. S.; Soper, A. K. *Inst. Phys. Conf. Ser.* **1990**, *107*, 193.
(30) Keen, D. A. *J. Appl. Crystallogr.* **2001**, *34*, 172.
(31) McGreevy, R. L. *J. Phys.: Condens. Matter* **2001**, *13*, R877.
(32) Tucker, M. G.; Keen, D. A.; Dove, M. T.; Goodwin, A. L.; Hui, Q. *J. Phys.: Condens. Matter* **2007**, *19*, 335218.
(33) Gonze, X.; Amadon, B.; Anglade, P. M.; Beuken, J.-M.; Bottin, F.; Boulanger, P.; Bruneval, F.; Caliste, D.; Caracas, R.; Cote, M.; Deutsch, T.; Genose, L.; Ghosez, P. H.; Giantomassi, M.; Goedecker, S.; Hamann, D.; Hermet, P.; Jollet, F.; Jomard, G.; Leroux, S.; Mancini, M.; Mazevet, S.; Oliveira, M. J. T.; Onida, G.; Pouillon, Y.; Rangel, T.; Rignanese, G.-M; Sangalli, D.; Shaltaf, R.; Verstraete, M.; Zerah, G.; Zwanziger, J. W. *Comput. Phys. Commun.* **2009**, *180*, 2582.
(34) Perdew, J. P.; Wang, Y. *Phys. Rev. B* **1992**, *45*, 13244.
(35) Ceperley, D. M.; Alder, B. J. *Phys. Rev. Lett.* **1980**, *45*, 566.
(36) Trouiller, N; Martins, J. L. *Phys. Rev. B* **1991**, *43*, 1993.
(37) Fuchs, M.; Scheffler, M. *Comput. Phys. Commun.* **1999**, *119*, 67.
(38) Monkhorst, H. J.; Pack, J. D. *Phys. Rev. B* **1976**, *13*, 5188.
(39) Gonze, X.; Lee, C. *Phys. Rev. B* **1997**, *55*, 10355.
(40) Cardona, M.; Güntherodt, G. *Light scattering in solids II*; Springer: Berlin, 1982.
(41) Hermet, P.; Izard, N.; Rahmani, A.; Ghosez, Ph. *J. Phys. Chem. B* **2006**, *110*, 24869.
(42) Nunes, R.; Gonze, X. *Phys. Rev. B* **2001**, *63*, 155107.
(43) Veithen, M.; Gonze, X.; Ghosez, Ph. *Phys. Rev. B* **2005**, *71*, 125107.
(44) Dove, M. T.; Keen, D. A.; Hannon, A. C.; Swainson, I. P. *Phys. Chem. Miner.* **1997**, *24*, 311.
(45) Keen, D. A.; Dove, M. T. *J. Phys.: Condens. Matter* **1999**, *11*, 9263.
(46) Tucker, M. G.; Dove, M. T.; Keen, D. A. *J. Phys.: Condens. Matter* **2000**, *12*, L723.
(47) Dean, K. J.; Sherman, W. F.; Wilkinson, G. R. *Spectrochim. Acta, Part A* **1982**, *38*, 1105.
(48) Sharma, S. K. *Vib. Spectra Struct.* **1989**, *17B*, 513.
(49) Gillet, P.; Le Cléac'h, A.; Madon, M. *J. Geophys. Res.* **1990**, *95*, 21635.
(50) Castex, J.; Madon, M. *Phys. Chem. Miner.* **1995**, *22*, 1.
(51) Schmidt, C.; Ziemann, M. A. *Am. Mineral.* **2000**, *85*, 1725.
(52) Etchepare, J.; Merian, M.; Smetankine, L. *J. Chem. Phys.* **1974**, *60*, 1873.